Chapter 1
Two-Dimensional Transition Metal Dichalcogenides: An Overview

Tao Liang, Yu Cai, Hongzheng Chen and Mingsheng Xu

Abstract Two-dimensional materials attract enormous research attentions owing to the fascinating properties and great potential applications in electronics, optoelectronics, spintronics, energy conversion, and storage. Among them, two-dimensional transitional metal dichalcogenides exhibit exceptional properties such as tunable bandgaps, phase transition, and superconductivity. As such, two-dimensional transitional metal dichalcogenides have been extensively studied focusing on the property, synthesis, modification, and devices. Furthermore, the combination of different two-dimensional transitional metal dichalcogenides brings in versatile functionalities and the proof-of-concept electrical devices such as tunneling field-effect transistors, light-emitting diodes and photovoltaics have been demonstrated in the planar or vertical heterostructures. Thus in this chapter, we summarize the basic knowledge and previous research results about the two-dimensional transitional metal dichalcogenides, emphasizing the atom structure, band structure, and electrical applications.

1.1 Introduction

Since graphene was first isolated from highly oriented pyrolytic graphite (HOPG) in 2004 [1], the excellent properties of graphene are motivating rapidly growing research enthusiasms in the layered materials, especially when they are thinned down to the atomic thickness. For layered transition metal dichalcogenides (TMDs), two-dimensional (2D, referring to few-layer and monolayer herein) ones exhibit distinct

T. Liang · M. Xu (✉)
State Key Laboratory of Silicon Materials, College of Information Science and Electronic Engineering, Zhejiang University, Hangzhou 310027, People's Republic of China
e-mail: msxu@zju.edu.cn

T. Liang · H. Chen
Department of Polymer Science and Engineering, Zhejiang University, Hangzhou 310027, People's Republic of China

Y. Cai
Department of Chemical and Biological Engineering, University of Colorado Boulder, Boulder, CO 80309-0596, USA

© Springer Nature Singapore Pte Ltd. 2019

N. S. Arul and V. D. Nithya (eds.), *Two Dimensional Transition Metal Dichalcogenides*,
https://doi.org/10.1007/978-981-13-9045-6_1

IIIB	IVB	VB	VIB	VIIB	VIII	VIII	VIII	IB	IIB	VIA
21 Sc	22 Ti	23 V	24 Cr	25 Mn	26 Fe	27 Co	28 Ni	29 Cu	30 Zn	16 S
39 Y	40 Zr	41 Nb	42 Mo	43 Tc	44 Ru	45 Rh	46 Pd	47 Ag	48 Cd	34 Se
57 La	72 Hf	73 Ta	74 W	75 Re	76 Os	77 Ir	78 Pt	79 Au	80 Hg	52 Te

Fig. 1.1 Known layered TMDs in the periodic table highlighted with shadow

properties from the bulk counterparts owing to the quantum confinement effect and broken inversion symmetry.

Thus, increasing research efforts are devoting to this field, and the fantastic properties of 2D TMDs are continuously being revealed. Depending on the filling state for the *d* band of the metal elements, 2D TMDs can be semiconductors with varied band structures, semimetals, true metals, and superconductors, which determine their roles in the electronic devices. The already known layered TMDs are outlined in a periodic table with shadow background (Fig. 1.1), and a majority of their 2D counterparts have been theoretically predicted and experimentally synthesized. In this chapter, the atoms arrangement, band structure, and electronic applications of the most studied 2D TMDs are reviewed. Other aspects of the 2D TMDs such as synthesis methods, characterization technique, application in catalysts, and heterostructure assembly can be found in details in the following chapters. The readers can also refer to a comprehensive review for more information about 2D materials [2].

1.2 Group VIB TMDs (MoS_2, WS_2, $MoSe_2$, WSe_2, $MoTe_2$, WTe_2)

1.2.1 Atoms Arrangement and Band Structure

As one of the most widely studied group VIB TMDs in the twentieth century, MoS_2 attracted a lot of research interest focusing on its tribological properties [3]. The renewed research interest in group VIB MX_2 (M = Mo and W, X = S, Se, and Te) following the discovery of graphene concentrates upon the electronic and catalytic properties of 2D counterparts. The tunable bandgap, high carrier mobility, and large surface area of 2D MX_2 render them potential application in electronics [4], optoelectronics [5], and catalysts [6]. Moreover, the reduced dimension along the vertical direction provides an ideal platform to study solid-state physics such as robust excitonic effects [7], spin-orbit coupling [8, 9], and many-body interactions [10], which are difficult to be observed in the bulk materials.

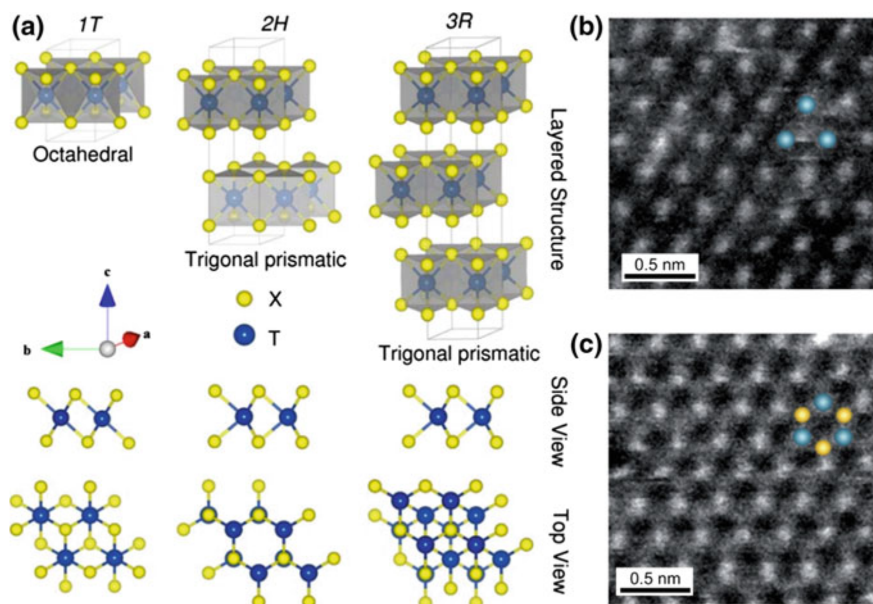

Fig. 1.2 **a** Ball-and-stick model of 1T, 2H, and 3R polymorphs of group VI TMDs [14]. Reproduced by permission of the Royal Society of Chemistry. **b**, **c** Atomic resolution STEM images of 1T (**b**) and 1H (**c**) phase of monolayer MoS_2. Blue and yellow balls represent Mo and S atoms, respectively [15]. Copyright 2013. Reprinted with permission from Macmillan Publishers

In similarity to graphite, MX_2 monolayers are held together by interlayer van der Waals (vdW) force to construct the bulk materials. The vdW force is several orders of magnitude weaker than the in-plane covalent bonding, making it feasible to obtain the monolayers through top-down routes including mechanical and liquid exfoliation. As such, most of the early theory verification and demonstration of proof-of-concept electronic devices based on 2D MX_2 were realized through this route [4, 5, 8, 11–13]. Different from the planar carbon sp^2 hybridization within each graphene layer, monolayer MX_2 is in fact composed of three sublayers of atoms, with one metal (M) sublayer sandwiched between two sublayers of chalcogenide (X) atoms, as shown in Fig. 1.2a [14]. Each M atom is sixfold coordinated with X atoms, forming either trigonal prismatic or octahedral geometry. In the trigonal prismatic atom arrangement, the above three X atoms are vertically above the below ones, while they stagger in the octahedral geometry.

The bulk MoS_2 shows polymorphs depending on the atoms arrangement in each monolayer and the relative position between monolayers. The three most commonly observed polymorphs of MoS_2 are 1T, 2H, and 3R. The number (1, 2, and 3) represents the layer number in the unit cell, and the letter stands for symmetry (T-trigonal, H-hexagonal, and R-rhombohedral). Figure 1.2b and c shows the atomic resolution scanning transmission electron microscopy (STEM) images for monolayer 1T and 1H MoS_2, respectively [15], consistent with the corresponding ball-and-stick model

in Fig. 1.2a. For sulfide and selenide, the 2H phase is stable, and the 1T phase is metastable, while for telluride, the 1T phase is more energetically favorable. The 2H phase could be converted to 1T phase under certain conditions, such as Li-ion intercalation, strain, electron beam, laser beam irradiation, as well as plasma bombardment. Conversely, the 1T phase could also be converted to 2H phase [16–20]. The most prominent feature of the group VIB TMDs is the layer-dependent band structure tunability. In the bulk materials, they own an indirect bandgap, which changes to direct one when being thinned down to monolayer limit [11].

Figure 1.3a–c shows the MoS_2 band structure of varied layer numbers calculated by density functional theory (DFT) [21]. In the bulk form, MoS_2 owns an indirect bandgap of about 1.2 eV. The valence band maximum (VBM) locates at the Γ point, and the conduction band minimum (CBM) locates in the middle of Γ-K direction in the Brillouin zone (Fig. 1.3a). As the layer number reduces, the VBM and CBM shift due to quantum confinement effects (Fig. 1.3b). A direct bandgap of about 1.9 eV is finally achieved in monolayer MoS_2 with both VBM and CBM sitting in the Brillouin zone K point (Fig. 1.3c). Other group VIB TMDs exhibit similar band structure evolution as a function of layer number [21–24]. Figure 1.3d shows the calculated band structure of monolayer WS_2 [21]. A direct bandgap of ~2.1 eV is predicted, in contrast to the ~1.3 eV indirect bandgap in the bulk form [21].

As a result of the band structure evolution, the photoluminescence (PL) emission dramatically increases when layer reduces (Fig. 1.3e). The PL quantum yield in monolayer MoS_2 is 100-fold higher than bilayer MoS_2 and four orders of magnitude higher than bulk MoS_2 (inset in Fig. 1.3e). Similarly, the electroluminescence (EL) efficiency in monolayers is also higher than the bulk materials [12], due to more efficient exciton generation and photon emission. The monolayer bandgap in the range of 1–2 eV, corresponding to the visible and near infrared spectrum range, and the direct bandgap nature render monolayer group VIB TMDs for constructing high-efficiency photodetectors, photovoltaics, and light-emitting diodes.

1.2.2 Electronics

2D group VIB TMDs are promising candidates for next-generation high-performance transistor channel materials, ascribing to the high conductivity, atomic thickness, and ultra-flat surface without dangling bonds. The first monolayer MoS_2 field-effect transistor (FET) is reported by Kis et al. [4]. The cross-sectional view of the device structure and the electrical connection (Fig. 1.4a), and the transfer and output curves of the device are displayed in Fig. 1.4b.

From the curves, field-effect electron mobility of ~200 cm^2/Vs and current on/off ratio exceeding 1×10^8 were extracted. The mobility is significantly boosted compared with its mostly reported 1–10 cm^2/Vs on SiO_2, ascribing to the suppression of Coulomb scattering by the top deposited HfO_2 layer. Fuhrer and Hone [25] pointed out that the capacitive coupling between the top and bottom gates could result in an overestimation of the mobility and the true mobility is likely in the range of

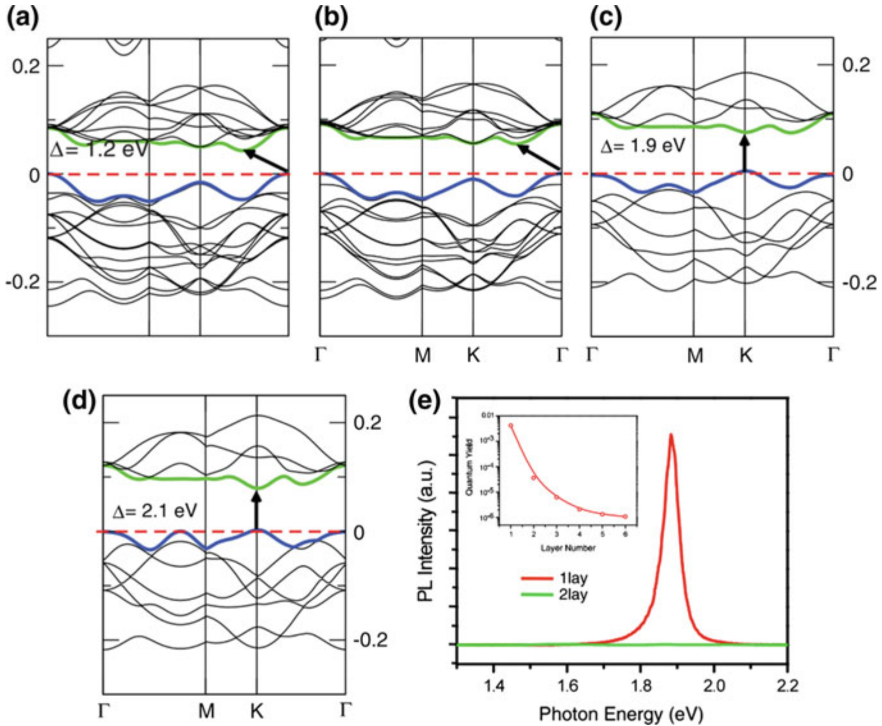

Fig. 1.3 **a**–**d** DFT calculated band structure of bulk MoS_2 (**a**), bilayer MoS_2 (**b**), monolayer MoS_2 (**c**), and monolayer WS_2 (**d**). The arrows indicate the fundamental bandgap, and the horizontal dashed lines indicate the Fermi level [21]. Copyright 2011 by the American Physical Society. Reproduced with permission (**e**) PL spectra for mono- and bilayer MoS_2 samples. The inset shows the PL quantum yield as a function of layer number [11]. Copyright 2010. Reproduced with permission from American Physical Society

2–7 cm^2/Vs. And thus Hall effect measurements were later performed, from which the mobility, contact resistance, and capacitive coupling can be obtained simultaneously [25]. One device exhibited mobility of 168 cm^2/Vs at 4 K and 60 cm^2/Vs at 250 K [25]. Other factors besides Coulomb scattering such as defects, charged impurities, and metal–semiconductor contact are also liable for the measured relatively low mobility in a FET device compared with the theoretical phonon-limited value. For example, through a thiol chemistry route to repair the sulfur vacancies and interface modification, Wang et al. achieved >80 cm^2/Vs electron mobility in monolayer MoS_2 bottom-gated FET [26].

To reduce the Schottky barrier height at the interface between metal electrode and MoS_2 channel, Chhowalla et al. [16] converted part of the MoS_2 flake underneath the metal electrodes from 2H to 1T phase, decreasing the contact resistance from 0.7–10 kΩ µm to 200–300 Ω µm.

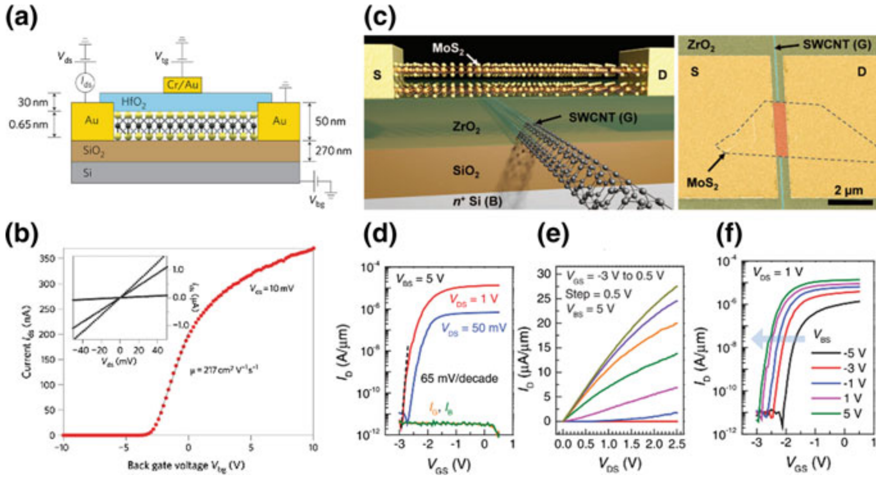

Fig. 1.4 **a** Cross-sectional view of the monolayer MoS_2 FET and the electrical connection for measurement. **b** Room temperature transfer and output (inset) curves for the monolayer MoS_2 FET. The transfer curve is obtained at $V_{ds} = 10$ mV, and the output curves are obtained at $V_{bg} = 0$, 1 and 5 V [4]. Reprinted by permission from Macmillan Publishers Ltd., copyright (2011) **c** 3D schematic (left) and false-colored SEM image (right) of MoS_2 FET with SWCNT gate. **d** I_D-V_{GS} curves of a bilayer MoS_2 FET at $V_{BS} = 5$ V and $V_{DS} = 50$ mV and 1 V. **e** I_D-V_{DS} curves for the device at $V_{BS} = 5$ V and varying V_{GS}. **f** I_D-V_{GS} curves at $V_{DS} = 1$ V and varying V_{BS} [36]. Copyright 2010. Reproduced with permission from AAAS

As a consequence, excellent device performance including high mobility, high on/off current ratio, current saturation, and low subthreshold swing (SS) was realized. Similarly, graphene was tested as an electrode material for MoS_2 FET to realize an ohmic contact [27]. Duan et al. devised an electrode transfer method to address the problem of Fermi-level pinning at the metal–semiconductor interface [28]. Instead of the conventionally evaporated metal electrodes, the transferred metal pads which are vdW interacted with the pre-deposition MoS_2 channel exhibited prominent advantages in maintaining the integrity of the underlying channel material and eliminating metal–semiconductor chemical bonding. The Fermi-level pinning in MoS_2 channel is eliminated and the metal–semiconductor Schottky barrier height is tuned and predicted by Schottky–Mott model. High electron mobility of 260 cm^2/Vs and hole mobility of 175 cm^2/Vs were realized by choosing metals electrodes with appropriate work functions [28]. The electrical performance of MoS_2 FETs is also closely correlated with the layer number and the substrate [29–31]. Compared with MoS_2, the electrical performances of other 2D group VIB TMDs are less investigated. However, they were proposed to exhibit superior electrical performance dictated by the theoretical calculation and existing experimental studies [32–35].

As the traditional silicon-based metal-oxide-semiconductor FET (MOSFET) scales down to the limit, the short channel effects become adversely prominent. Benefiting from the ultrathin and surface bonding-free nature, the 2D group VIB

TMDs are promising candidates to construct high-performance FETs at a reduced channel length. To implement such a conception, a single-walled carbon nanotube (SWCNT) was used as the bottom gate to tune the bilayer MoS_2 FET (Fig. 1.4c) [36]. The effective channel length was about 1 nm in the on state and 3.9 nm in the off state inferred from the simulation. Figure 1.4d–f shows the electrical performance of the MoS_2 FETs gated by SWCNT at a short channel length. A nearly ideal SS of ~65 mV per decade at room temperature and on/off current ratio of ~10^6 were realized. More complicated device components in logical circuits were also devised and preliminarily tested based on group VIB TMDs FET [37–40].

1.2.3 Photo-, Chemical, and Bio- Sensors

The high performance of 2D group VIB TMDs FETs, as well as the large exposed surface, provides a good platform for their applications in sensing light, chemicals, and biomaterials, through a stimulus to electrical signal switch process. For most of the sensing devices based on 2D materials FETs, the change of the carrier concentration in the channel material upon applying a stimulus is responsible for the electrical response, similar to the function of a top gate. The first single-layer MoS_2 phototransistor was reported by Zhang et al. [5] and a photoresponsivity of 7.5 mA/W and a prompt response time of ~50 ms were achieved.

Later, high photoresponsivities of 880 and 2200 A/W were reported by Kis et al. [41] and Li et al. [42], respectively. Figure 1.5a shows a schematic of the single-layer MoS_2 phototransistor and Fig. 1.5b shows the source-drain current versus source-drain voltage (I_{ds}-V_{ds}) curves of the phototransistor under dark and different illumination intensities. The increased current with the illumination intensity was ascribed to the photoelectric and photo-thermoelectric effects [43, 44]. The monolayer MoS_2 FET is also suitable for detection of chemical vapors, especially those of electron donors (Fig. 1.5c). Figure 1.5d shows the conductivity change of monolayer MoS_2 channel upon exposing to a sequence of 0.002% P_0 triethylamine pulses (black line). The amplitude of conductivity change was in proportion to triethylamine concentration and the control experiment of exposure to nitrogen and water vapor confirmed that the observed response was due to interaction of the MoS_2 with triethylamine. The MoS_2 sensor is less sensitive to electron acceptors, owing to the weak n-type nature of the MoS_2 flakes. The MoS_2 FET for label-free bio-detection was also demonstrated [46]. In this device architecture (Fig. 1.5e), the MoS_2 channel was covered with a dielectric layer, which was functionalized with receptors for explicitly capturing the target biomolecules.

When the target biomolecule was captured by the receptor biomolecule, it would induce a gating effect and modulate the current between the source and drain electrodes. Figure 1.5f shows the I_{ds}-V_{gs} (gate voltage) curves of the MoS_2 biosensor at three PH values of the solution. At low PH value (PH = 3), the surface OH groups of the dielectric layer tended to be protonated, causing a positive surface charge and reduced threshold voltage. The source-drain current (I_{ds}) increased with the decrease

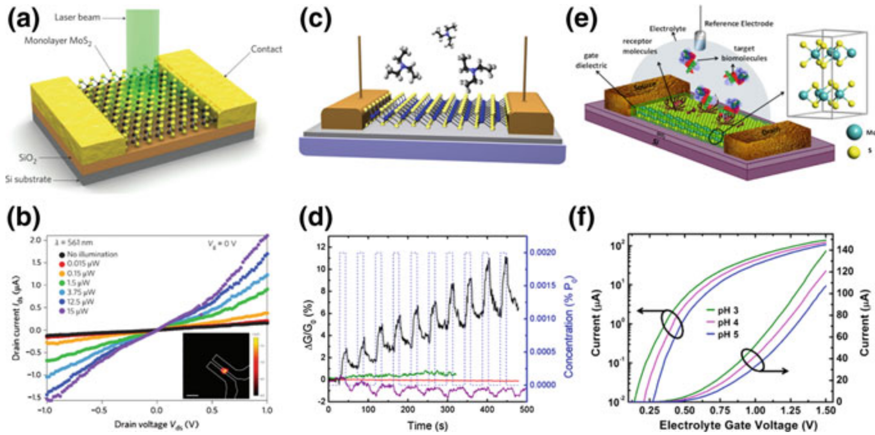

Fig. 1.5 **a** Schematic of the single-layer MoS_2 phototransistor. **b** I_{ds}-V_{ds} curves of the phototransistor under dark and different illumination intensities. The inset image shows the spatial photocurrent map by raster-scanning of a focused laser beam over the device. Scale bar, 5 μm [41]. Copyright (2013). Reprinted with permission from Macmillan Publishers **c** Schematic of the device structure of monolayer MoS_2 chemical sensor. **d** Conductivity variation of monolayer MoS_2 sensor channel upon exposing to a sequence of 0.002% P_0 triethylamine pulses (black line). The dashed blue line shows the pulse timing (15 s on/30 s off) and concentration. The solid red and green lines show the response to nitrogen and water vapor (0.025% P_0), respectively. The purple line shows the response of graphene sensor to water vapor pulses (0.025% P_0) [45]. Copyright 2013 American Chemical Society. Published with permission **e** Schematic of the device structure of MoS_2 biosensor. **f** I_{ds}-V_{gs} curves of the MoS_2 biosensor at three PH values of the solution [46]. Copyright 2014. Reproduced with permission from American Chemical Society

in pH value. The sensitivity as high as 713 for a pH change by 1 unit in the subthreshold region and a wide operable pH range from 3 to 9 were demonstrated. This kind of MoS_2 biosensor was also used for specific protein detection at an ultralow concentration [46].

1.2.4 Tunneling FET

Tunneling FETs (TFET) have been realized in graphene-based van der Waals heterostructures [47, 48]. In those work, 2D MoS_2 or WS_2 layers were inserted between the graphene layers, acting as atomically thin barrier. High-performance TFET characteristics were obtained in such a device structure. Banerjee et al. [49] devised a novel TFET utilizing band-to-band tunneling (BTBT). The device structure is shown in Fig. 1.6a. Under a bias, electrons flow from degenerately doped p-type Ge to the MoS_2 channel in a BTBT way and diffuse to the drain electrode.

In the off state, only the electrons above the conduction band of Ge could move to MoS_2 according to the band alignment between Ge and MoS_2. The current was

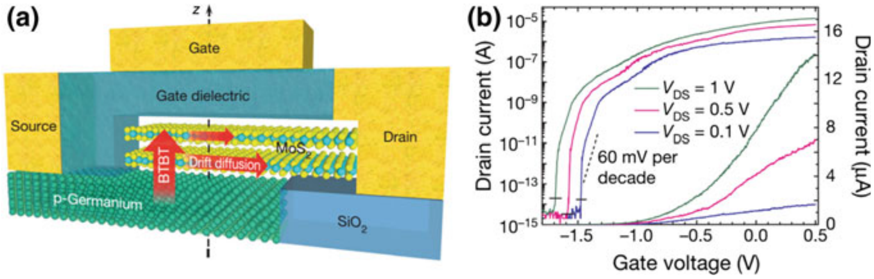

Fig. 1.6 **a** Schematic of the band-to-band tunneling FET. The red arrows show the electron transport path. The electrons band-to-band tunnel (BTBT) from Ge source to MoS_2 channel, and laterally diffuse to the drain electrode. **b** I_{ds}-V_{gs} curves for three different drain voltages of 0.1, 0.5, and 1 V, from which the SS were obtained [49]. Copyright (2015). Reproduced with permission from Macmillan Publishers

low due to the lack of available electrons in the conduction band. As the gate voltage was increased, the MoS_2 conduction band was lowered below the Ge valence band. The electrons in the Ge valence band could flow to the empty states in the MoS_2 channel, leading to an abrupt increase in current. The drain current as a function of gate voltage at three different drain voltages is shown in Fig. 1.6b. Ultralow SS all below 60 mV per decade over about four decades of current were deduced from the three curves, breaking the fundamental limitations on SS in MOSFETs.

1.2.5 Light Emitters and Photovoltaics

Similar to the PL, EL in 2D group VIB TMDs originates from the excitonic recombination. They are supposed to exhibit more efficient light emission being direct bandgap semiconductors in the monolayer limit. In a pioneer work by Steiner et al. [12], a pair of electrodes were deposited and contacted with the single-layer MoS_2. Electrons were injected from one electrode to the conduction band of MoS_2 and combined with holes, forming excitons under a high source-drain voltage. This is known as a hot carrier process, and the light emission is localized in the vicinity of the contacts. 2D p-n junction is more efficient in exciton generation and requires a reduced source-drain bias. Three independent groups reported the construction of 2D p-n junctions within monolayer WSe_2 through local electrostatic doping [50–52]. WSe_2 is selected owing to the ambipolar transport behaviors.

Figure 1.7a shows the device structure of monolayer WSe_2 with two split gates [51]. The two gates could locally dope the channel. When the same polar voltage was applied to the two gates, the devices operated as a resistor (blue and green dash lines in Fig. 1.7b). Whereas when the two gates were applied voltage of opposite polarity, the current rectification was observed (blue and green solid lines in Fig. 1.7b). Thus,

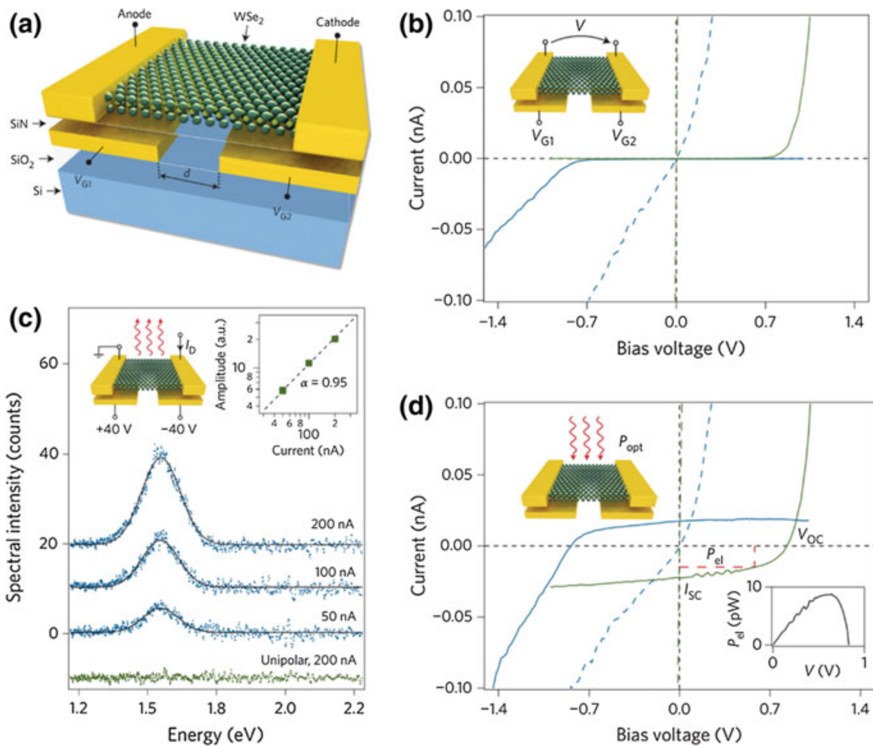

Fig. 1.7 **a** Schematic of the monolayer WSe_2 device with split-gate electrodes. **b** I–V curves of the device in the dark under different biasing conditions: p-n (solid green line; $V_{G1} = -40$ V, $V_{G2} = 40$ V), n–p (solid blue line; $V_{G1} = 40$ V, $V_{G2} = -40$ V), n–n (dashed green line; $V_{G1} = V_{G2} = 40$ V), p–p (dashed blue line; $V_{G1} = V_{G2} = -40$ V). **c** Electroluminescence emission spectra recorded at constant currents of 50, 100, and 200 nA, respectively. The green curve shows that no light emission is obtained under unipolar conduction. The left inset shows the two gate voltages and the right inset shows that the amplitude of the emission intensity on a double-logarithmic scale is linearly dependent on the current. **d** *I*–*V* curves of the device under illumination. The biasing conditions are the same as (**b**). Inset: electrical power (P_{el}, operating as a diode) versus voltage [51]. Copyright (2014). Reproduced with permission from Macmillan Publishers

the device could operate as a light emitter when a forward current is driven through the device and opposite voltages are applied to the two gates.

Figure 1.7c shows the EL emission spectra at different driving currents. The EL emission is found at the same energy as the PL and the emission intensity increases linearly with the driving current (inset in Fig. 1.7c), indicating that the EL arises from excitonic transition. Vertically standing van der Waals heterostructures are also good platforms for investigating the light emission behaviors of 2D semiconductors. In this kind of structure, the carriers flow perpendicular to the 2D plane. Compared with the planar structure where the carriers flow within the 2D plane, the vertical

structure offers the advantages such as reduced contact resistance, higher current density, and whole device light emission.

For example, a sandwich structure of graphene/BN/MoS_2/BN/graphene was devised [53]. The Fermi level of the two graphene layers could be tuned to align with the conduction and valence band edges of MoS_2, resulting in electrons and holes injection through the BN barrier. EL emission with external quantum efficiency of ~10% was realized. The 2D semiconductors could also be attempted as a light absorption layer in a photovoltaic device. For instance, asymmetric electrodes of Pd and Au were applied in a MoS_2 FET [54]. When the channel was illuminated by light, the generated electron-hole pairs could be separated under the influence of the built-in potential from the space charge at the contacts, giving rise to a photovoltaic effect. The 2D p-n heterostructure could be another viable way for electron-hole pair generation and separation. When the device in Fig. 1.7 was illuminated with light and the two split gates were applied by opposite voltages, a photovoltaic effect was observed (green and blue solid lines in Fig. 1.7d). The power conversion efficiency (PCE) of the device was 0.5% with a filling factor (FF) of 50%. The comparatively low PCE and FF are ascribed to the low absorption of the atomically thin photoactive layer. The strategy of combining 2D TMDs with plasmonic materials or tandem device structure for sufficient light absorption would be used to improve photo-to-electric conversion performance. Other n-type and p-type 2D TMDs would also be combined to construct the p-n junction to fulfill the photovoltaic functionalities [55].

1.2.6 Valleytronics

2D group VIB TMDs also provide a good platform for the study of valley physics. In monolayer group VIB TMDs with broken inversion symmetry, the valence bands are split by spin-orbit coupling. The spin splitting must be opposite at the two inequivalent valleys, labeled K and K' in the first Brillouin zone (Fig. 1.8a). Right (left)-handed circularly polarized light only couples to the K (K′) valleys according to the optical selection rules [56, 57], as has been experimentally demonstrated by valley polarization using polarization resolved PL (Fig. 1.8b) [8, 9, 58, 59]. The circularly polarized EL emission, which is electrically switchable, was also demonstrated in a WSe_2 p-i-n junction [60]. The p- and n-regions are defined by the electric double layer at the electrolyte-solid interface, which could induce a large gate field and break the inversion symmetry of few-layer WSe_2. Figure 1.8c shows the circularly polarized EL emission for two opposite current flow directions. The circular polarization was reversed when the source-drain bias was exchanged. The result was explained by the electron-hole overlap controlled by in-plane electric field [60].

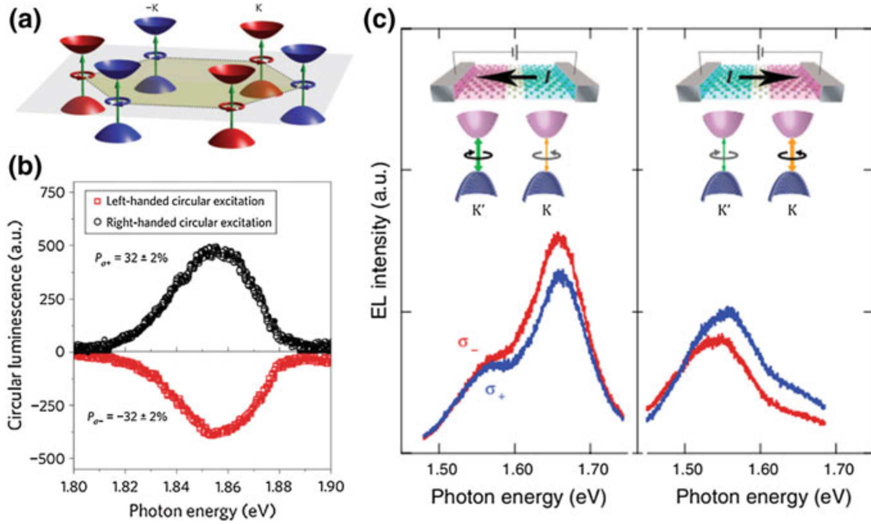

Fig. 1.8 **a** Valley contrasting optical selection rules in a 2D hexagonal lattice with broken inversion symmetry [57]. Reprinted by permission from Macmillan Publishers Ltd., copyright (2014). **b** Polarization resolved PL spectra under circularly polarized excitation [8]. Reprinted by permission from Macmillan Publishers Ltd., copyright (2012). **c** Circularly polarized EL spectra for two opposite current directions. The contribution to EL from two valleys is shown in the bottom [60]. Copyright 2014. Reprinted with permission from Science

1.3 Group VIIB TMDs (ReS_2 and $ReSe_2$)

1.3.1 Atoms Arrangement and Band Structure

Rhenium dichalcogenide (ReX_2, X = S and Se) is a representative-layered group VIIB TMD, although the element Re is discovered late [61]. Similar to group VIB TMDs, the ReX_2 layers are held together by weak vdW force and the Re and X atoms within each layer are covalently bonded.

The difference is that the extra electron in each Re atom brings in a chemical bond between Re atoms. Each four Re atoms arrange in a parallelogram shape and the parallelograms connect to form atomic chains along the principle *b*-axis, which is the shortest axis in the basal plane (Fig. 1.9a) [62]. The *a*-axis is 118.97° apart from the *b*-axis, corresponding to the second-shortest axis. This kind of atoms arrangement of both ReS_2 and $ReSe_2$ is experimentally verified by aberration-corrected STEM, as shown in Fig. 1.9b and c [63]. For ReS_2, the distance between two neighboring parallelograms in the direction of *b* and *a* is measured as 0.34 and 0.31 nm, and that for $ReSe_2$ is 0.39 and 0.35 nm, respectively, in agreement with the theoretical calculations [64].

Unlike the stable H phase observed in MX_2 (M = Mo and W, X = S and Se), ReX_2 shows a distorted 1T structure originating from the Peierls distortion [65], which

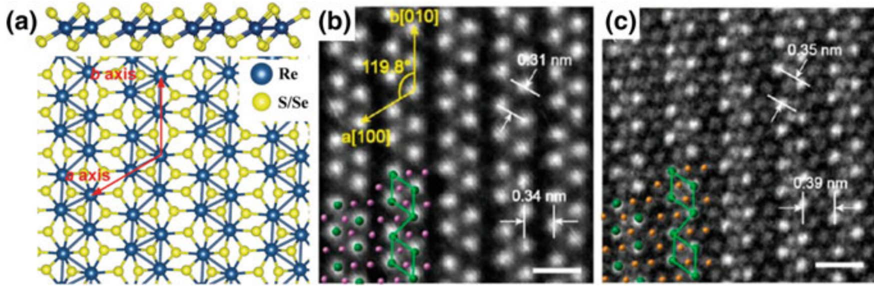

Fig. 1.9 **a** Side view (top panel) and top view (bottom panel) of the atoms arrangement in monolayer ReX_2 (X = S and Se) [62]. Reproduced with permission from Wiley-VCH Verlag GmbH (**b**, **c**) ADF STEM images of monolayer ReS_2 (**b**) and $ReSe_2$ (**c**) [63]. Copyright 2015. Reprinted with permission from American Chemical Society

prevents interlayer-ordered stacking and minimizes the wavefunctions overlap. As a result, the interlayer interaction in ReX_2 is over an order of magnitude lower than that in MoS_2 (18 vs. 460 mV per unit cell). The bulk ReX_2 behaves like vibrationally and electronically decoupled while stacked monolayer counterparts [65]. Thus the bulk ReX_2 can be directly used for study of 2D physics, circumventing the necessity of preparing monolayer samples. The bandgap of layered TMDs is strongly influenced by the layer number. For group VIB TMDs, an indirect to direct bandgap transition occurs when the bulk materials are thinned down to monolayer limit, caused by the exciton confinement effects [11]. As a consequence, both the PL quantum yield and PL emission position vary. However, for ReX_2, the electronic band structure is barely influenced by the layer number, due to the weak interlayer interaction.

Figure 1.10a shows the band structure for monolayer, trilayer, and five-layer ReS_2 by ab initio calculation [66]. The CBM and VBM share the identical position in the Brillouin zone, respectively, giving rise to direct bandgap for monolayer, trilayer, and five-layer ReS_2. The bandgap only varies slightly, from 1.44 eV for monolayer ReS_2, 1.40 eV for trilayer ReS_2, to 1.35 eV for five-layer ReS_2. In fact, the bulk ReS_2 is also a direct bandgap semiconductor with a bandgap of 1.35 eV, predicted by generalized gradient approximation (GGA) [67]. As such, the PL emission for ReS_2 with different layer numbers is a superposition of the emission from individual monolayers. The PL intensity increases as the layer number increases and no significant emission position change is observed due to the similar bandgap (Fig. 1.10b) [65].

1.3.2 Anisotropic Optical and Electrical Properties

Deriving from the atoms arrangement, ReX_2 crystals are supposed to exhibit anisotropic optical and electrical response behaviors. The anisotropic properties of the bulk materials have been documented [68, 69] and that of the few-layer and

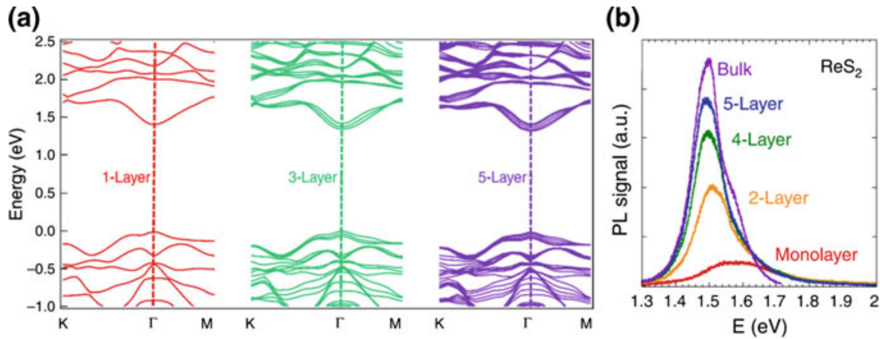

Fig. 1.10 **a** Ab initio calculated band structures of monolayer, trilayer, and five-layer ReS_2 [66]. Reprinted by permission from Macmillan Publishers Ltd., copyright (2015). **b** PL signal of ReS_2 with different layer numbers [65]. Copyright 2014. Reprinted with permission from Macmillan Publishers

monolayer counterparts are the current research focus. The unique anisotropy is not only important for the understanding of physical properties but also fundamental for designing novel kinds of electronic devices.

The anisotropic Raman response of ReX_2 is revealed in several studies [70–73]. Compared with the group VIB TMDs, the Raman spectra of ReX_2 exhibit more bands due to its low symmetry. Figure 1.11a shows an optical image of ReS_2 samples with varied layer numbers obtained by mechanical exfoliation [70]. The Raman spectra for the 1L, 2L, 3L, and 4L ReS_2 are shown in Fig. 1.11b. Note that the peak position of Raman mode I continuously changes with the layer number, from 133.1 ± 0.1 cm^{-1} in the 1L to 136.2 ± 0.2 cm^{-1} in the 4L, while the position of modes III, IV, and V barely varies. Thus the peak position difference between Raman mode I and other modes, such as mode III, can be used to identify ReS_2 layer number in few-layered samples, similar to the work done on MoS_2 [74]. Figure 1.11c exhibits the orientation-dependent polarization response of mode V in the 4L region with unpolarized (black), cross-polarized (blue), and parallel-polarized (red) collection. The cross- and parallel-polarized spectra yield 4-lobed and 2-lobed shapes, respectively, indicating the anisotropic Raman response behavior of thin ReS_2 by angle-resolved polarized Raman spectroscopy technique.

1.3.3 Anisotropic Electrical Properties

The unique atomic structure also renders an anisotropic electron transport behavior for 2D ReX_2. The theoretical calculations have predicted that the conductivity along *b*-axis is higher than other directions [68, 69]. The FET devices were fabricated with the electrodes patterning perpendicular to the ReS_2 *a*- and *b*-axes, respectively, and the transfer curves are shown in Fig. 1.12a [66].

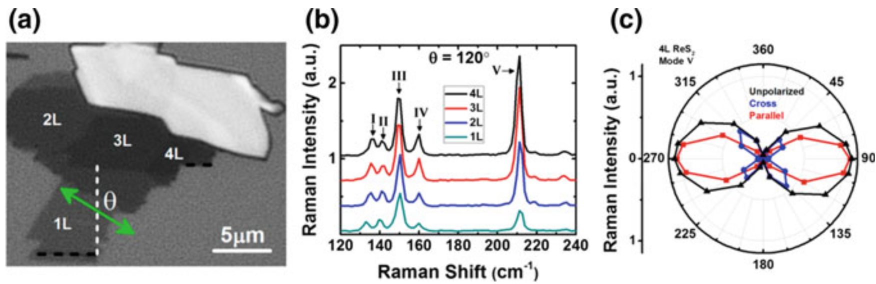

Fig. 1.11 **a** Optical microscopy image of a mechanical-exfoliated ReS_2 sample with 1-4 layers identified. **b** Raman spectra taken in the 1L, 2L, 3L, and 4L ReS_2 regions with an orientation of $\theta = 120°$. **c** Raman intensity of mode V in the 4L region with unpolarized (black), cross-polarized (blue), and parallel-polarized (red) collection [70]. Copyright 2015. Reproduced with permission from American Chemical Society

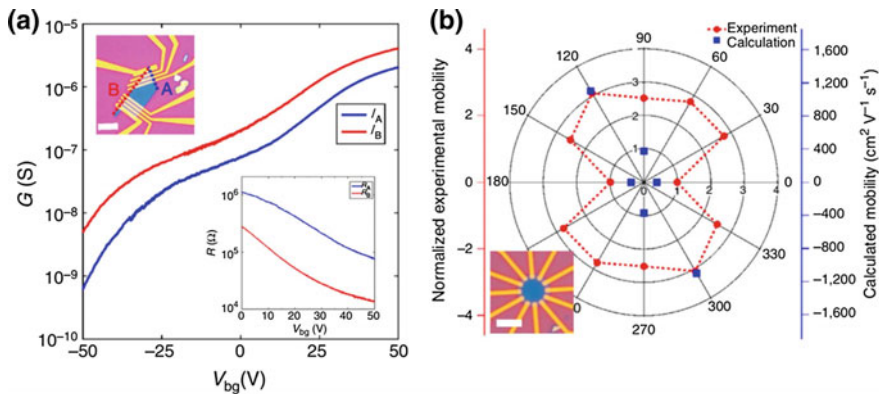

Fig. 1.12 **a** Transfer curves of a quadrilateral-shaped five-layer ReS_2 flake in the A and B directions. The left inset shows the optical microscopy image of the FET device, scale bar, 10 mm, and the right inset shows the four-probe resistance of the same devices as a function of V_{bg}. **b** Experimentally measured field-effect mobilities of a six-layer ReS_2 device along 12 evenly spaced directions in polar coordinate. The blue dots show the calculated mobilities in the same polar coordinate. The optical image of the device is shown inset [66]. Copyright 2015. Reprinted with permission from Macmillan Publishers

Obviously, the current along the *b*-axis is higher than that along the *a*-axis, and the current ratio was also gate dependent. To eliminate the contact resistance, the four-probe resistance was measured (inset in Fig. 1.12a) and the result was consistent with the current trend.

The anisotropic transport behaviors were further evaluated by the device shown in the inset of Fig. 1.12b. The 12 electrodes were separated by 30° apart. The transfer curves of each pair of diagonally positioned electrodes were measured, and the normalized mobility was plotted in a polar coordinate. The field-effect mobility is highly angle dependent and the largest value is 60° from the direction with the

lowest value. The anisotropic ratio of mobility was ~3.1, which is larger than 1.8 for anisotropic black phosphorus [75].

1.3.4 Electronics and Optoelectronic Devices

Since ReX_2 sheets have exhibited a high room temperature mobility above 30 cm^2/Vs and a high on/off current ratio of over 10^6 [76, 77], they are promising for application in electronics. As the synthesis technology for ReX_2 is rapidly developing, especially the controlled sample preparation by CVD with predefined layer number and size [78–81], increasingly more electronic devices based on these materials are emerging. Figure 1.13 shows some elementary logical gates constructed with few-layer ReS_2 channel [82]. Monolayer graphene was applied as the source, drain, and gate electrode, and a kind of ion gel with a high capacitance was used as the dielectric layer.

The graphene electrodes avoid the trap states and Fermi-level pinning in the ReS_2 channel, and the ion gel can tune the electron concentration of the channel within a large range. Figure 1.13a shows an optical image of the logical NOT device and Fig. 1.13b exhibits the reasonable voltage transfer characteristics and the voltage gain exceeding 3.5. For the NAND gate, three transistors are connected in series (Fig. 1.13c). When either or both of the inputs are in the logic states "0," the V_{out} is in the logic state "1," and the V_{out} logic state "0" is only achieved when both the inputs are held at "1" (Fig. 1.13e). For the NOR gate, one transistor is connected in series with two transistors connecting in parallel (Fig. 1.13d). When either or both of the inputs are in the logic states "1," the V_{out} is in the logic state "0," and the V_{out} logic state "1" is only achieved when both the inputs are held at "0" (Fig. 1.13e).

Since the direct bandgap nature of ReX_2 is independent of the layer number, highly performance photodetectors are expected in the few-layer samples owing to improved light absorption compared with the monolayers. A similar device structure designed for group VIB TMDs is also utilized for ReX_2 photodetectors, and high device performance was reported [77, 81, 83–87]. The polarization-sensitive photoresponsivity originating from the high in-plane optical anisotropy was also observed in a $ReSe_2$ photodetector [84]. The EL was also preliminarily proposed and reported in ReS_2 [88] and ReS_2 p-n junction [89], and more efforts are necessary in this area to realize devices with higher performance.

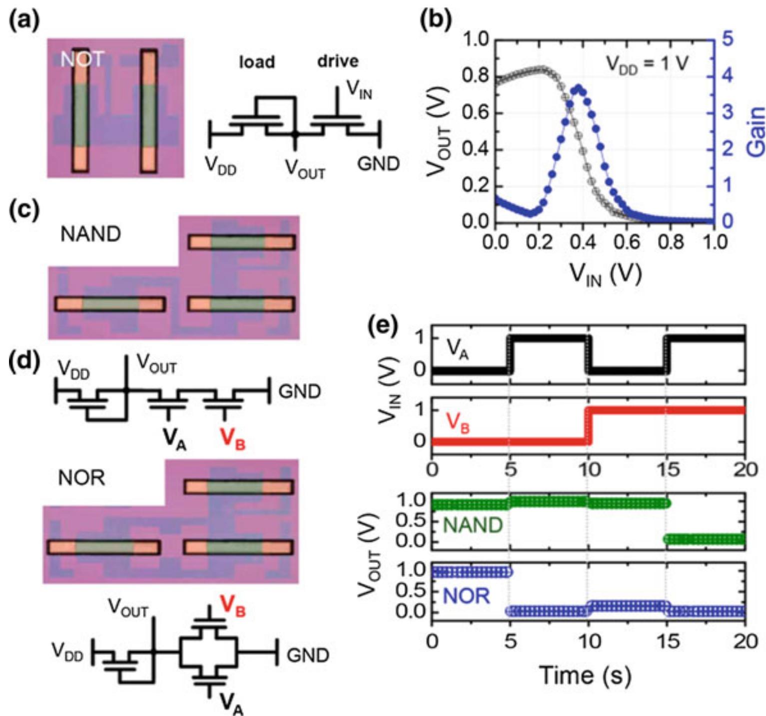

Fig. 1.13 **a** Optical image and schematic band diagram of the NOT gate. **b** Voltage transfer characteristics and signal gain of the NOT gate. (**c**, **d**) Optical images and schematic band diagrams of the **c** NAND and **d** NOR gates. **e** The input and output voltages of the NAND and NOR gates as a function of time [82]. Copyright 2017. Reproduced with permission from American Chemical Society

1.4 Group VIII TMDs (PtS_2 and $PtSe_2$)

1.4.1 Atoms Arrangement and Band Structure

PtX_2 (X = S and Se) crystal possesses a typical 1T-type hexagonal crystal structure, similar to the 1T phase of group VIB TMDs. The Pt atom is in a tilted octahedral site and coordinated by six X atoms. The lattice constants of the hexagonal structure are defined in Fig. 1.14a [90]. Figure 1.14b shows an atom-resolved STEM image of few-layer $PtSe_2$ [91]. The atoms can be clearly identified from the image contrast and the intensity profile along the red line. The fast Fourier transform image is also in agreement with the hexagonal structure of $PtSe_2$. Different from the weak interlayer interaction in group VIIB TMDs and the moderate interlayer interaction in group VIB TMDs as discussed above, the interaction between PtX_2 layers is strong, resulting from the overlapping of the p_z orbital of interlayer X atoms [90–95].

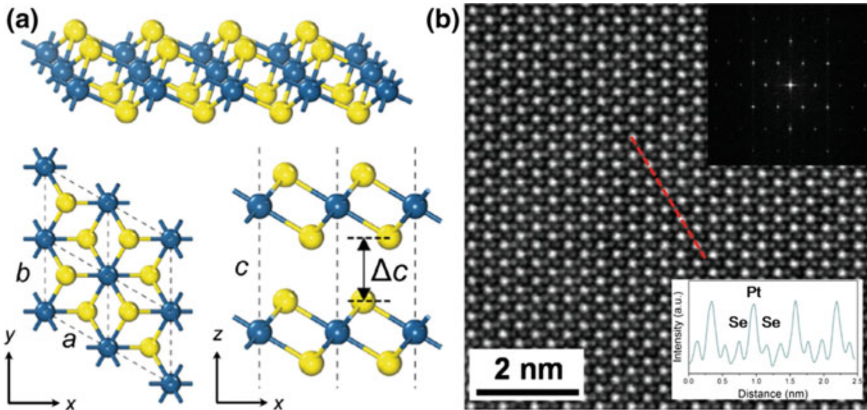

Fig. 1.14 **a** 3D, top, and side view of the 1T PtX_2 (X = S and Se). The blue and yellow balls represent Pt and X atoms, respectively [90]. Reproduced with permission from Wiley-VCH Verlag GmbH **b** Atoms resolved STEM image of few-layer $PtSe_2$. The up inset is the fast Fourier-transformed image showing hexagonal structure and the bottom inset shows the intensity line proline along the red line [91]. Copyright 2017. Reproduced with permission from Wiley-VCH Verlag GmbH

As a result, the band structure of PtX_2 changes dramatically with the layer number. Monolayer $PtSe_2$ is a semiconductor with indirect bandgap. The bandgap narrows in the bilayer and becomes zero in the trilayer, as predicted by the first-principle calculation (Fig. 1.15a–c) [96].

Also, the indirect bandgap could be transformed to direct bandgap under strain [93]. PtS_2 shares a similar band structure evolution with $PtSe_2$ as a function of layer number. The experimentally verified and DFT calculated bandgaps versus number of layers are plotted in Fig. 1.15d [90]. The layer-dependent semiconductor to metal transition is unique in the group VIII TMDs. Note that the value of the bandgap varies depending on the calculation method and the level of theory, as well as the defect concentration [90–96].

1.4.2 Electronic Devices

PtX_2 is predicted to exhibit phonon-limited carrier mobility exceeding 1000 cm^2/Vs at room temperature [97]. Thus they are suitable for high-speed electronic devices. The FETs based on different layer numbers of PtS_2 and $PtSe_2$ were constructed and tested [90, 91]. The output and transfer curves for an 11-nm-thick $PtSe_2$ device are shown in Fig. 1.16a and b. The I_{ds} increased with the positive back gate voltage , indicating the n-type carrier transport. The room temperature electron mobility derived from the linear region of the transfer curve was 210 cm^2/Vs. This mobility is much higher than that of 2D group VIB and VIIB TMDs. Moreover, the device is rather stable, which exhibits negligible degradation after storing in air for one

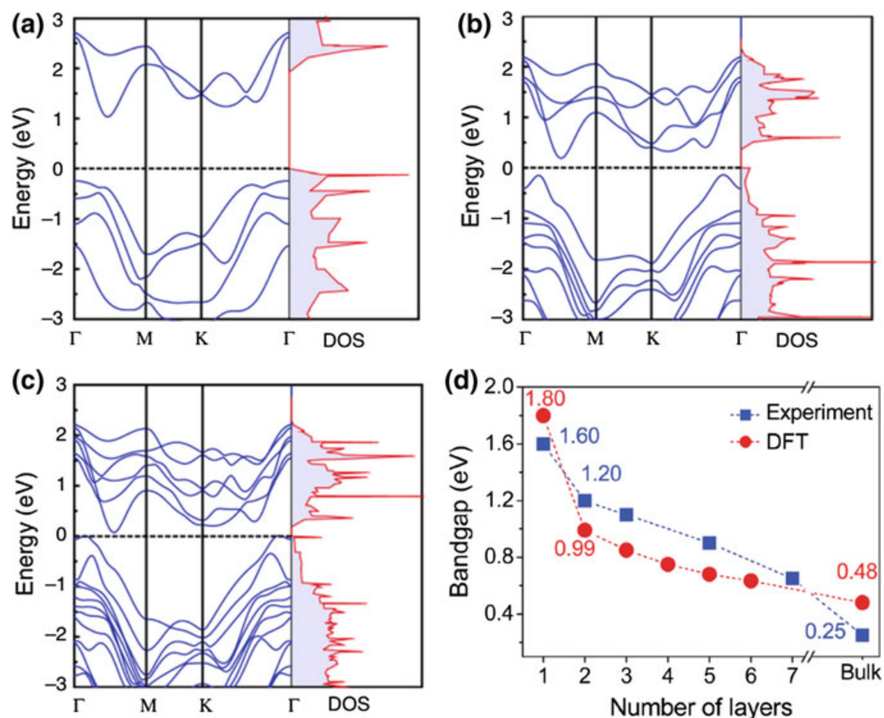

Fig. 1.15 **a**–**c** First-principle calculated band structure of defect-free **a** monolayer, **b** bilayer, and **c** trilayer $PtSe_2$ [96]. Reprinted by permission from Macmillan Publishers Ltd., copyright (2018), **d** Experimentally measured and DFT calculated bandgap as a function of PtS_2 layer number [90]. Copyright 2016. Reproduced with permission from Wiley-VCH Verlag GmbH

year [91]. A FET fully composed of $PtSe_2$ was also reported [98]. A thinner $PtSe_2$ sheet is used as a semiconductor channel material, and the thicker $PtSe_2$ sheet is used as an electrode. The same kind of material within one device yields an Ohmic contact between electrode and channel, which is beneficial for carrier injection. P-type carrier transport was also reported in $PtSe_2$ FET [99]. The different 2H phase resulted from the different synthesis route may be accounted for the observed p-type carrier transport. Photodetectors using the planar FET device configuration based on PtX_2 channel materials have also been realized [91, 96, 98], in analogy to the photodetectors based on group VIB and VIIB TMDs.

The unique advantages for group VIII TMDs photodetectors are the tunable narrow bandgaps, which is an excellent choice for mid-infrared light detection. Figure 1.16c and d shows the time-resolved photocurrent when the device was illuminated with lasers of different wavelengths. For the monolayer $PtSe_2$ FET, a photoresponsivity of 0.9 and 0.15 A W^{-1} was obtained for 632 nm and 1.47 μm illumination, respectively. However, the device showed negligible photoresponse to

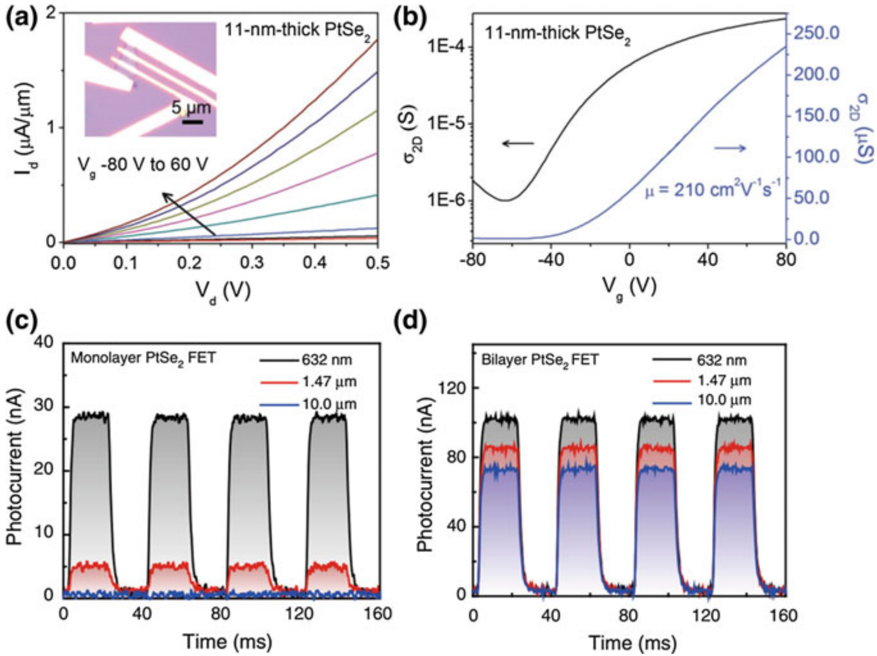

Fig. 1.16 **a**, **b** Output and transfer curves of a 11 nm $PtSe_2$ transistor. The optical image of the device is shown in the inset in (**a**) [91]. Reproduced with permission from Wiley-VCH Verlag GmbH (**c**, **d**) Time-resolved photocurrent of **c** monolayer and **d** bilayer $PtSe_2$ FET at a bias voltage of 0.1 V and zero gate voltage under laser illumination with a wavelength of 632 nm, 1.47 μm, and 10 μm, respectively [96]. Copyright (2018) Reproduced with permission from Macmillan Publishers

a mid-infrared laser illumination ($\lambda = 10$ μm) since the photon energy of the incident laser is far below the bandgap of monolayer $PtSe_2$ (Eg ~ 1.2 eV).

For the bilayer $PtSe_2$ FET, a much higher photoresponsivity of 6.25, 5.5, and 4.5 A W^{-1} was observed for 632 nm, 1.47 μm, and 10 μm illumination, respectively. The broadband mid-infrared photoresponse of bilayer $PtSe_2$ FET was proposed to be originated from the defect-induced bandgap reduction [96]. The $PtSe_2$ FET could also be used as a NO_2 gas sensor [100], in which ultrahigh sensitivity and extremely fast response time are obtained.

A photovoltaic device was proposed and fabricated by transferring $PtSe_2$ thin films onto pre-patterned Si substrates [100], forming $PtSe_2$/n-Si Schottky barrier diodes (SBDs). The schematic of the device structure is shown in Fig. 1.17a and the rectifying characteristics are shown in Fig. 1.17b. A clear photoresponse was observed in the reverse bias region under illumination, as shown in Fig. 1.17c. The energy band diagram at the junction of the SBD under illumination is presented in Fig. 1.17d. J-V curves of the devices with different $PtSe_2$ thicknesses under an incident light intensity (P_{in}) of 4.7 mW/cm^2 are plotted in Fig. 1.17e. As the thickness

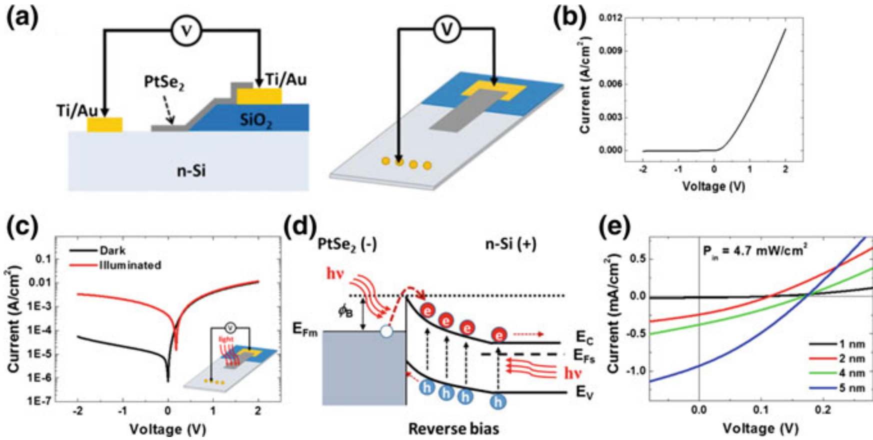

Fig. 1.17 **a** Schematic of the $PtSe_2$/n-Si Schottky barrier diode. **b** J-V curve of the device with a $PtSe_2$ film synthesized from 4-nm-thick Pt on a linear scale. **c** J-V curves of the device with a $PtSe_2$ film synthesized from 4-nm-thick Pt on a semilogarithmic scale under dark and illumination. **d** Energy band diagram of the Schottky junction between $PtSe_2$ and n-Si under reverse bias. **e** J–V characteristics of the devices with different $PtSe_2$ thicknesses under an incident light intensity (P_{in}) of 4.7 mW/cm^2 [100]. Copyright 2016. Reprinted with permission from American Chemical Society

of the $PtSe_2$ layer increases, light absorption enhances and thus the power conversion efficiency increases.

1.5 Other 2D TMDs

In addition to the TMDs discussed above, more 2D TMDs are emerging and attracting increasing attentions. These materials exhibit dramatically different properties mainly due to the varied *d*-orbit electron states of the transition metals and provide versatile platforms for studying fundamental physical conceptions such as charge density wave (CDW), phase transition, and superconductivity.

In the group VB TMDs, VX_2 ($X = S$ and Se) exhibits intrinsic ferromagnetic behaviors and the magnetic moments and strength of magnetic coupling could be tuned by isotropic strain, as predicted by the first-principles calculations [101]. The ferromagnetism has been experimentally verified in both VS_2 and VSe_2 [102, 103]. The CDW behavior was also discovered in VSe_2 [103] and the CDW transition temperature is dependent on the thickness [104, 105]. For VS_2, the stable phase (H or T) relies on the temperature and the thickness [106]. Few-layer VS_2 is metallic [107, 108] and the metal-insulator transition is also observed and influenced by the vdW interaction [108].

The DFT calculation reveals that bulk and few-layers VSe_2 in T and H phase, and monolayer VSe_2 in T phase are metallic, while the H monolayer is a semi-

conductor [109]. 2D $NbSe_2$ is also investigated and the coexistence of CDW and superconducting phase has been observed in monolayer limit [110]. The electronic phase transitions can be achieved by electrostatic gating [111]. A plenty of low-temperature electronic states also appear in 1T-TaS_2, especially the first reported superconductivity in a pristine 1T-TaS_2 [112]. A series of phase transitions in 1T-TaS_2 thin flakes are reported by gate electric field induced Li-ion intercalation [113]. For 2H TaS_2, the superconductivity persists down to 3.5 nm, and the critical temperature increases from 0.5 to 2.2 K as the layers are thinned down [114]. Similarly, the CDW and superconductivity phases were also reported in 2D group IVB TMDs, like $TiSe_2$ [115–117]. The transition temperature could be tuned by the electric field [116]. 2D $HfSe_2$ in group IVB TMDs is a kind of n-type semiconductor, with a relatively small bandgap of ~1.1 eV revealed by scanning tunneling spectroscopy (STS) on a molecular beam epitaxy grown sample [118] and high phonon-limited mobility over 3500 cm^2/Vs predicted by calculation [97].

1.6 Conclusions

In this chapter, the atomic arrangement, band structure, and electronic applications of most of the widely studied 2D TMDs are summarized. Differentiating from graphene and bulk TMDs, 2D TMDs exhibit unique properties and application potential. As the synthesis technique is continuously developing, more 2D TMDs are obtained. For example, 47 kinds of binary, alloy, and heterostructured 2D TMDs have been synthesized by a salt-assisted CVD method in a recent report [119]. The availability of these materials paves the way for a deeper understanding of the physical origins and device applications. At the same time, apart from the optical and electrical applications, 2D magnetism is attracting increasing attentions, exhilarated by the particular magnetic properties discovered in transition metal Cr based 2D materials [120, 121]. As such, low-power and ultra-compact spintronic applications could be expected based on 2D TMDs.

Acknowledgements The work was partially supported by the financial support of the National Natural Science Foundation of China (Grant 51472219 and 51672244).

References

1. Novoselov KS, Geim AK, Morozov SV, Jiang D, Zhang Y, Dubonos SV et al (2004) Electric field effect in atomically thin carbon films. Science 306:666–669
2. Xu M, Liang T, Shi M, Chen H (2013) Graphene-like two-dimensional materials. Chem Rev 113:3766–3798
3. Winer WO (1967) Molybdenum disulfide as a lubricant: a review of the fundamental knowledge. Wear 10:422–452

4. Radisavljevic B, Radenovic A, Brivio J, Giacometti V, Kis A (2011) Single-layer MoS_2 transistors. Nat Nanotechnol 6:147–150
5. Yin Z, Li H, Li H, Jiang L, Shi Y, Sun Y et al (2012) Single-layer MoS_2 phototransistors. ACS Nano 6:74–80
6. Li H, Tsai C, Koh AL, Cai L, Contryman AW, Fragapane AH et al (2016) Activating and optimizing MoS_2 basal planes for hydrogen evolution through the formation of strained sulphur vacancies. Nat Mater 15:48–53
7. Ugeda MM, Bradley AJ, Shi SF, da Jornada FH, Zhang Y, Qiu DY et al (2014) Giant bandgap renormalization and excitonic effects in a monolayer transition metal dichalcogenide semiconductor. Nat Mater 13:1091–1095
8. Zeng H, Dai J, Yao W, Xiao D, Cui X (2012) Valley polarization in MoS_2 monolayers by optical pumping. Nat Nanotechnol 7:490–493
9. Mak KF, He K, Shan J, Heinz TF (2012) Control of valley polarization in monolayer MoS_2 by optical helicity. Nat Nanotechnol 7:494–498
10. Qiu DY, da Jornada FH, Louie SG (2013) Optical spectrum of MoS_2 : many-body effects and diversity of exciton states. Phys Rev Lett 111:216805
11. Mak KF, Lee C, Hone J, Shan J, Heinz TF (2010) Atomically thin MoS2: a new direct-gap semiconductor. Phys Rev Lett 105:136805
12. Sundaram RS, Engel M, Lombardo A, Kruple R, Ferrari AC, Avouris P et al (2013) Electroluminescence in single layer MoS_2. Nano Lett 13:1416–1421
13. Xia F, Wang H, Xiao D, Dubey M, Ramasubramaniam A (2014) Two-dimensional material nanophotonics. Nat Photonics 8:899–907
14. Kuc A (2014) Low-dimensional transition-metal dichalcogenides. Royal Soc Chem, Cambridge, pp 1–29
15. Chhowalla M, Shin HS, Eda G, Li LJ, Loh KP, Zhang H (2013) The chemistry of two-dimensional layered transition metal dichalcogenide nanosheets. Nat Chem 5:263–275
16. Kappera R, Voiry D, Yalcin SE, Branch B, Gupta G, Mohite AD, Chhowalla M (2014) Phase-engineered low-resistance contacts for ultrathin MoS_2 transistors. Nat Mater 13:1128–1134
17. Cho S, Kim S, Kim JH, Zhao J, Seok J, Keum DH et al (2015) Phase patterning for ohmic homojunction contact in $MoTe_2$. Science 349:625–628
18. Song S, Keum DH, Cho S, Perello D, Kim Y, Lee YH (2016) Room temperature semiconductor–metal transition of $MoTe_2$ thin films engineered by strain. Nano Lett 16:188–193
19. Scalise E, Houssa M, Pourtois G, Afanasev V, Stesmans A (2012) Strain-induced semiconductor to metal transition in the two-dimensional honeycomb structure of MoS_2. Nano Res 5:43–48
20. Zhu J, Wang Z, Yu H, Li N, Zhang J, Meng J, Liao M et al (2017) Argon plasma induced phase transition in monolayer MoS_2. J Am Chem Soc 139:10216–10219
21. Kuc A, Zibouche N, Heine T (2011) Influence of quantum confinement on the electronic structure of the transition metal sulfide TS_2. Phys Rev B 83:245213
22. Zhao W, Ghorannevis Z, Chu L, Toh M, Kloc C, Tan PH et al (2013) Evolution of electronic structure in atomically thin sheets of WS_2 and WSe_2. ACS Nano 7:791–797
23. Ruppert C, Aslan OB, Heinz TF (2014) Optical properties and band gap of single- and few-layer $MoTe_2$ crystals. Nano Lett 14:6231–6236
24. Roldán R, Silva-Guillén JA, López-Sancho MP, Guinea F, Cappelluti E, Ordejob P (2014) Electronic properties of single-layer and multilayer transition metal dichalcogenides MX_2 (M = Mo, W and X = S, Se): electronic properties of TMDs. Ann Phys 526:347–357
25. Fuhrer MS, Hone J (2013) Measurement of mobility in dual-gated MoS_2 transistors. Nat Nanotechnol 8:146–147
26. Yu Z, Pan Y, Shen Y, Wang Z, Ong ZY, Xu T, Xin R et al (2014) Towards intrinsic charge transport in monolayer molybdenum disulfide by defect and interface engineering. Nat Commun 5:5290–5297
27. Guimarães MHD, Gao H, Han Y, Kang K, Xie S, Kim CJ et al (2016) Atomically thin ohmic edge contacts between two-dimensional materials. ACS Nano 10:6392–6399

28. Liu Y, Guo J, Zhu E, Liao L, Lee SJ, Ding M et al (2018) Approaching the Schottky-Mott limit in van der Waals metal–semiconductor junctions. Nature 557:696–700
29. Das S, Chen HY, Penumatcha AV, Appenzeller J (2013) High performance multilayer MoS_2 transistors with scandium contacts. Nano Lett 13:100–105
30. Bao W, Cai X, Kim D, Sridhara K, Fuhrer MS (2013) High mobility ambipolar MoS_2 field-effect transistors: Substrate and dielectric effects. Appl Phys Lett 102:042104
31. Zheng J, Yan X, Lu Z, Qiu H, Xu G, Zhou X et al (2017) High-mobility multilayered MoS_2 flakes with low contact resistance grown by chemical vapor deposition. Adv Mater 29:1604540
32. Huang JK, Pu J, Hsu CL, Chiu MH, Juang ZY, Chang YH et al (2014) Large-area synthesis of highly crystalline WSe_2 monolayers and device applications. ACS Nano 8:923–930
33. Zhou J, Liu F, Lin J, Huang X, Xia J, Zhang B et al (2017) Large-area and high-quality 2D transition metal telluride. Adv Mater 29:1603471
34. Empante TA, Zhou Y, Klee V, Nguyen AE, Lu IH, Valentin MD et al (2017) Chemical vapor deposition growth of few-layer $MoTe_2$ in the 2H, 1T′, and 1T phases: tunable properties of $MoTe_2$ films. ACS Nano 11:900–905
35. Nakaharai S, Yamamoto M, Ueno K, Lin YF, Li SL, Tsukagoshi K (2015) Electrostatically reversible polarity of ambipolar α-$MoTe_2$ transistors. ACS Nano 9:5976–5983
36. Desai SB, Madhvapathy SR, Sachid AB, Llinas JP, Wang Q, Ahn GH, Pinter G et al (2016) MoS_2 transistors with 1-nanometer gate lengths. Science 354:99–102
37. Radisavljevic B, Whitwick MB, Kis A (2011) Integrated circuits and logic operations based on single-layer MoS_2. ACS Nano 5:9934–9938
38. Cheng R, Jiang S, Chen Y, Liu Y, Weiss N, Cheng HC et al (2014) Few-layer molybdenum disulfide transistors and circuits for high-speed flexible electronics. Nat Commun 5:5143
39. Wang H, Yu L, Lee YH, Shi Y, Hsu A, Chin ML et al (2012) Integrated circuits based on bilayer MoS_2 transistors. Nano Lett 12:4674–4680
40. Yu L, El-Damak D, Radhakrishna U, Ling X, Zubair A, Lin Y et al (2016) Design, modeling, and fabrication of chemical vapor deposition grown MoS_2 circuits with E-mode FETs for large-area electronics. Nano Lett 16:6349–6356
41. Lopez-Sanchez O, Lembke D, Kayci M, Radenovic A, Kis A (2013) Ultrasensitive photodetectors based on monolayer MoS_2. Nat Nanotechnol 8:497–501
42. Zhang W, Huang JK, Chen CH, Chang YH, Cheng YJ, Li LJ (2013) High-gain phototransistors based on a CVD MoS_2 monolayer. Adv Mater 25:3456–3461
43. Wu CC, Jariwala D, Sangwan VK (2013) Elucidating the photoresponse of ultrathin MoS_2 field-effect transistors by scanning photocurrent microscopy. J Phys Chem Lett 4:2508–2513
44. Buscema M, Barkelid M, Zwiller V, van der Zant HSJ, Steele GA, Castellanos-Gomez A (2013) Large and tunable photothermoelectric effect in single-layer MoS_2. Nano Lett 13:358–363
45. Perkins FK, Friedman AL, Cobas E, Campbell PM, Jernigan GG, Jonker BT (2013) Chemical vapor sensing with monolayer MoS_2. Nano Lett 13:668–673
46. Sarkar D, Liu W, Xie X (2014) MoS_2 field-effect transistor for next-generation label-free biosensors. ACS Nano 8:3992–4003
47. Britnell L, Gorbachev RV, Jalil R, Belle BD, Schedin F, Mishchenko A et al (2012) Field-effect tunneling transistor based on vertical graphene heterostructures. Science 335:947–950
48. Georgiou T, Jalil R, Belle BD, Britnell L, Gorbachev RV, Morozov SV et al (2013) Vertical field-effect transistor based on graphene–WS_2 heterostructures for flexible and transparent electronics. Nat Nanotechnol 8:100–103
49. Sarkar D, Xie X, Liu W (2015) A subthermionic tunnel field-effect transistor with an atomically thin channel. Nature 526:91–95
50. Baugher BWH, Churchill HOH, Yang Y, Jarillo-Herrero P (2014) Optoelectronic devices based on electrically tunable p–n diodes in a monolayer dichalcogenide. Nat Nanotechnol 9:262–267
51. Pospischil A, Furchi MM, Mueller T (2014) Solar-energy conversion and light emission in an atomic monolayer p–n diode. Nat Nanotechnol 9:257–261

52. Ross JS, Klement P, Jones AM, Ghimire NJ, Yan J, Mandrus DG et al (2014) Electrically tunable excitonic light-emitting diodes based on monolayer WSe_2 p–n junctions. Nat Nanotechnol 9:268–272
53. Withers F, Del Pozo-Zamudio O, Mishchenko A, Rooney AP, Gholinia A, Watanabe K et al (2015) Light-emitting diodes by band-structure engineering in van der Waals heterostructures. Nat Mater 14:301–306
54. Fontana M, Deppe T, Boyd AK, Rinzan M, Liu AY, Paranjape M et al (2013) Electron-hole transport and photovoltaic effect in gated MoS_2 Schottky junctions. Sci Rep 3:1634
55. Furchi MM, Pospischil A, Libisch F, Burgdorfer J, Mueller T (2014) Photovoltaic effect in an electrically tunable van der Waals heterojunction. Nano Lett 14:4785–4791
56. Xiao D, Liu GB, Feng W, Xu X, Yao W (2012) Coupled spin and valley physics in monolayers of MoS_2 and other group-VI dichalcogenides. Phys Rev Lett 108:196802
57. Xu X, Yao W, Xiao D, Heinz TF (2014) Spin and pseudospins in layered transition metal dichalcogenides. Nat Phys 10:343–350
58. Cao T, Wang G, Han W, Ye H, Zhu C, Shi J et al (2012) Valley-selective circular dichroism of monolayer molybdenum disulphide. Nat Commun 3:887
59. Jones AM, Yu H, Ghimire NJ, Wu S, Aivazian G, Ross JS et al (2013) Optical generation of excitonic valley coherence in monolayer WSe_2. Nat Nanotechnol 8:634–638
60. Zhang YJ, Oka T, Suzuki R (2014) Electrically switchable chiral light-emitting transistor. Science 344:725–728
61. Rahman M, Davey K, Qiao SZ (2017) Advent of 2D rhenium disulfide (ReS_2): fundamentals to applications. Adv Funct Mater 27:1606129
62. Wen W, Zhu Y, Liu X, Hsu HP, Fei Z, Chen Y et al (2017) Anisotropic spectroscopy and electrical properties of 2D $ReS_{2(1-x)}Se_{2x}$ alloys with distorted 1T structure. Small 13:1603788
63. Lin YC, Komsa HP, Yeh CH, Bjorkman T, Liang ZY, Ho CH et al (2015) Single-layer ReS_2: two-dimensional semiconductor with tunable in-plane anisotropy. ACS Nano 9:11249–11257
64. Murray H, Kelly SP, Chianelli RR (1994) Structure of rhenium disulfide. Inorg Chem 33:4418–4420
65. Tongay S, Sahin H, Ko C, Luce A, Fan W, Liu K et al (2014) Monolayer behaviour in bulk ReS_2 due to electronic and vibrational decoupling. Nat Commun 5:3252
66. Liu E, Fu Y, Wang Y, Feng Y, Liu H, Wan X et al (2015) Integrated digital inverters based on two-dimensional anisotropic ReS_2 field-effect transistors. Nat Commun 6:6991
67. Gehlmann M, Aguilera I, Bihlmayer G, Nemsak S, Nagler P, Gospodaric P et al (2017) Direct observation of the band gap transition in atomically thin ReS_2. Nano Lett 17:5187–5192
68. Ho CH, Huang YS, Tiong KK (1999) In-plane anisotropy of the optical and electrical properties of layered ReS_2 crystals. J Phys: Condens Matter 11:5367
69. Ho CH, Huang YS, Tiong KK (2001) In-plane anisotropy of the optical and electrical properties of ReS_2 and $ReSe_2$ layered crystals. J Alloys Compd 222–226
70. Chenet DA, Aslan OB, Huang PY, Fan C, van der Zande AM, Heinz TF et al (2015) In-plane anisotropy in mono- and few-layer ReS_2 probed by Raman spectroscopy and scanning transmission electron microscopy. Nano Lett 15:5667–5672
71. Wolverson D, Crampin S, Kazemi AS, LLie A, Bending SJ (2014) Raman spectra of monolayer, few-layer, and bulk $ReSe_2$: an anisotropic layered semiconductor. ACS Nano 8:11154–11164
72. Feng Y, Zhou W, Wang Y, Zhou J, Liu E, Fu Y et al (2015) Raman vibrational spectra of bulk to monolayer ReS_2 with lower symmetry. Phys Rev B 92:054110
73. Lorchat E, Froehlicher G, Berciaud S (2016) Splitting of interlayer shear modes and photon energy dependent anisotropic Raman response in N-layer ReSe2 and ReS2. ACS Nano 10:2752–2760
74. Liu KK, Zhang W, Lee YH, Lin YC, Chang MT, Su CY et al (2012) Growth of large-area and highly crystalline MoS_2 thin layers on insulating substrates. Nano Lett 12:1538–1544
75. Xia F, Wang H, Jia Y (2014) Rediscovering black phosphorus as an anisotropic layered material for optoelectronics and electronics. Nat Commun 5:4458

76. Pradhan NR, McCreary A, Rhodes D, Lu Z, Feng S, Manousakis E et al (2015) Metal to insulator quantum-phase transition in few-layered ReS_2. Nano Lett 15:8377–8384
77. Corbet CM, McClellan C, Rai A (2015) Field effect transistors with current saturation and voltage gain in ultrathin ReS_2. ACS Nano 9:363–370
78. He X, Liu F, Hu P, Fu W, Wang X, Zeng Q et al (2015) Chemical vapor deposition of high-quality and atomically layered ReS_2. Small 11:5423–5429
79. Keyshar K, Gong Y, Ye G, Brunetto G, Zhou W, Cole DP et al (2015) Chemical vapor deposition of monolayer rhenium disulfide (ReS_2). Adv Mater 27:4640–4648
80. Cui F, Wang C, Li X, Wang G, Liu K, Yang Z et al (2016) Tellurium-assisted epitaxial growth of large-area, highly crystalline ReS_2 atomic layers on mica substrate. Adv Mater 28:5019–5024
81. Li X, Cui F, Feng Q, Wang G, Xu X, Wu J et al (2016) Controlled growth of large-area anisotropic ReS_2 atomic layer and its photodetector application. Nanoscale 8:18956–18962
82. Dathbun A, Kim Y, Kim S (2017) Large-area CVD-grown sub-2V ReS_2 transistors and logic gates. Nano Lett 17:2999–3005
83. Zhang E, Jin Y, Yuan X, Wang W, Zang C, Tang L et al (2015) ReS_2-based field-effect transistors and photodetectors. Adv Funct Mater 25:4076–4082
84. Zhang E, Wang P, Li Z, Wang C, Song C, Huang C et al (2016) Tunable ambipolar polarization-sensitive photodetectors based on high-anisotropy $ReSe_2$ nanosheets. ACS Nano 10:8067–8077
85. Hafeez M, Gan L, Li H (2016) Large-area bilayer ReS_2 film/multilayer ReS_2 flakes synthesized by chemical vapor deposition for high performance photodetectors. Adv Funct Mater 26:4551–4560
86. Shim J, Oh A, Kang DH, Oh S, Jang SK, Jeon J et al (2016) High-performance 2D rhenium disulfide (ReS_2) transistors and photodetectors by oxygen plasma treatment. Adv Mater 28:6985–6992
87. Yang S, Tongay S, Li Y (2014) Layer-dependent electrical and optoelectronic responses of $ReSe_2$ nanosheet transistors. Nanoscale 6:7226–7231
88. Gutiérrez-Lezama I, Reddy BA, Ubrig N, Morpurgo AF (2016) Electroluminescence from indirect band gap semiconductor ReS_2. 2D Mater 3:045016
89. Najmzadeh M, Ko C, Wu K Tongay S, Wu J (2016) Multilayer ReS_2 lateral p–n homojunction for photoemission and photodetection. Appl Phys Express 9:055201
90. Zhao Y, Qiao J, Yu P (2016) Extraordinarily strong interlayer interaction in 2D layered PtS_2. Adv Mater 28:2399–2407
91. Zhao Y, Qiao J, Yu Z, Hu Z, Lin Z, Lau SP et al (2017) High-electron-mobility and air-stable 2D layered $PtSe_2$ FETs. Adv Mater 29:1604230
92. Wang Y, Li L, Yao W, Song S, Sun JT, Pan J et al (2015) Monolayer $PtSe_2$, a new semiconducting transition-metal-dichalcogenide, epitaxially grown by direct selenization of Pt. Nano Lett 15:4013–4018
93. Miró P, Ghorbani-Asl M, Heine T (2014) Two dimensional materials beyond MoS_2: noble-transition-metal dichalcogenides. Angew Chem Int Ed 53:3015–3018
94. Rasmussen FA, Thygesen KS (2015) Computational 2D materials database: electronic structure of transition-metal dichalcogenides and oxides. J Phys Chem C 119:13169–13183
95. Guo GY, Liang WY (1986) The electronic structures of platinum dichalcogenides: PtS_2, $PtSe_2$, and $PtTe_2$. J Phys C: Solid State Phys 19:995
96. Yu X, Yu P, Wu X, Sing B, Zeng Q, Lin H, Zhou W et al (2018) Atomically thin noble metal dichalcogenide: a broadband mid-infrared semiconductor. Nat Commun 9:1545
97. Zhang W, Huang Z, Zhang W, Li Y (2014) Two-dimensional semiconductors with possible high room temperature mobility. Nano Res 7:1731–1737
98. Su TY, Medina H, Chen YZ, Wang SW, Lee SS, Shih YC, Chen CW et al (2018) Phase-engineered $PtSe_2$-layered films by a plasma-assisted selenization process toward all $PtSe_2$-based field effect transistor to highly sensitive, flexible, and wide-spectrum photoresponse photodetectors. Small 14:1800032

99. Wang Z, Li Q, Besenbacher F (2016) Facile synthesis of single crystal $PtSe_2$ nanosheets for nanoscale electronics. Adv Mater 28:10224–10229
100. Yim C, Lee K, McEvoy N, Brien MO, Riazimehr S, Berner NC et al (2016) High-performance hybrid electronic devices from layered $PtSe_2$ films grown at low temperature. ACS Nano 10:9550–9558
101. Ma Y, Dai Y, Guo M (2012) Evidence of the existence of magnetism in pristine VX_2 monolayers ($X = S, Se$) and their strain-induced tunable magnetic properties. ACS Nano 6:1695–1701
102. Gao D, Xue Q, Mao X, Wang W, Xu Q, Xue D (2013) Ferromagnetism in ultrathin VS_2 nanosheets. J Mater Chem C 1:5909–5916
103. Xu K, Chen P, Li X, Wu C, Guo Y, Zhao et al (2013) Ultrathin nanosheets of vanadium diselenide: a metallic two-dimensional material with ferromagnetic charge-density-wave behavior. Angew Chem Int Ed 52:10477–10481
104. Yang J, Wang W, Liu Y, Du H, Ning W, Zheng G et al (2014) Thickness dependence of the charge-density-wave transition temperature in VSe_2. Appl Phys Lett 105:063109
105. Zhang Z, Niu J, Yang P, Gong Y, Ji Q, Shi J et al (2017) Van der Waals epitaxial growth of 2D metallic vanadium diselenide single crystals and their extra-high electrical conductivity. Adv Mater 29:1702359
106. Zhang H, Liu LM, Lau WM (203) Dimension-dependent phase transition and magnetic properties of VS_2. J. Mater. Chem. A 1:10821–10828
107. Feng J, Sun X, Wu C (2011) Metallic few-layered VS_2 ultrathin nanosheets: High two-dimensional conductivity for in-plane supercapacitors. J Am Chem Soc 133:17832–17838
108. Guo Y, Deng H, Sun X, Li X, Zha J, Wu J et al (2017) Modulation of metal and insulator states in 2D ferromagnetic VS_2 by van der Waals interaction engineering. Adv Mater 29:1700715
109. Li F, Tu K, Chen Z (2014) Versatile electronic properties of VSe_2 bulk, few-layers, monolayer, nanoribbons, and nanotubes: A computational exploration. J Phys Chem C 118:21264–21274
110. Xi X, Zhao L, Wang Z (2015) Strongly enhanced charge-density-wave order in monolayer $NbSe_2$. Nat Nanotechnol 10:765–769
111. Xi X, Berger H, Forró L, Shan J, Mak KF (2016) Gate tuning of electronic phase transitions in two-dimensional $NbSe_2$. Phys Rev Lett 117:106801
112. Sipos B, Kusmartseva AF, Akrap A (2008) From Mott state to superconductivity in 1T-TaS_2. Nat Mater 7:960–965
113. Yu Y, Yang F, Lu XF, Yan YJ, Cho YH, Ma L Gate-tunable phase transitions in thin flakes of 1T-TaS_2. Nat Nanotechnol 10:270–276
114. Navarro-Moratalla E, Island JO, Mañas-Valero S, Pinilla-Cienfuegos E, Castellanos-Gomes A, Quereda J, Rubio-Bollinger G et al (2016) Enhanced superconductivity in atomically thin TaS_2. Nat Commun 7:11043
115. Chen P, Chan YH, Fang XY (2015) Charge density wave transition in single-layer titanium diselenide. Nat Commun 6:8943
116. Li LJ, O'Farrell ECT, Loh KP, Eda G, Ozyilmaz B, Castro Neto AH (2016) Controlling many-body states by the electric-field effect in a two-dimensional material. Nature 529:185–189
117. Sugawara K, Nakata Y, Shimizu R (2015) Unconventional charge-density-wave transition in monolayer 1T-TiSe2. ACS Nano 10:1341–1345
118. Yue R, Barton AT, Zhu H, Azcatl A, Pena LF, Wang J et al (2015) $HfSe_2$ thin films: 2D transition metal dichalcogenides grown by molecular beam epitaxy. ACS Nano 9:474–480
119. Zhou J, Lin J, Huang X, Zhou Y, Chen Y, Xia et al (2018) A library of atomically thin metal chalcogenides. Nature 556:355–359
120. Gong C, Li L, Li Z, Ji H, Stern A, Xia Y et al (2017) Discovery of intrinsic ferromagnetism in two-dimensional van der Waals crystals. Nature 546:265–269
121. Huang B, Clark G, Navarro-Moratalla E, Klein DR, Cheng R, Seyler KL et al (2017) Layer-dependent ferromagnetism in a van der Waals crystal down to the monolayer limit. Nature 546:270–273